Theory of EPR lineshape in samples concentrated in paramagnetic spins: Effect of enhanced internal magnetic field on high-field high-frequency (HFHF) EPR lineshape

Sushil K. Misra [a,*], Stefan Diehl [a,b]

[a] Physics Department, Concordia University, 1455 de Maisonneuve Boulevard West, Montreal, Quebec, Canada H3G 1M8
[b] Physikalisches Institut, Justus Liebig Universität, 35390 Gießen, Germany

ABSTRACT

A theoretical treatment is provided for the calculation of EPR (electron paramagnetic resonance) lineshape as affected by interactions with paramagnetic ions in the vicinity. The internal fields seen by the various paramagnetic ions due to interactions with paramagnetic ions in their vicinity, as well as the resulting lineshapes, become quite significant at high magnetic fields required in high-frequency (HFHF) EPR. The resulting EPR signals for the various ions are therefore characterized by different g-shifts and lineshapes, so that the overall EPR lineshape, which is an overlap of these, becomes distorted, or even split in HFHF EPR, from that observed at lower frequencies. The observed EPR lineshapes in $MnSO_4 \cdot H_2O$ powder and K_3CrO_8 single-crystal samples have been simulated here taking into account g-shifts and modified lineshapes. These simulations show that in these samples, concentrated in paramagnetic spins, the position and lineshapes of EPR signals are significantly modified in HFHF EPR involving very high magnetic fields.

© 2012 Elsevier Inc. All rights reserved.

1. Introduction

EPR (electron paramagnetic resonance) is a very sensitive technique to probe the environment of a paramagnetic ion, not possible with many common characterization techniques. This is why it has been exploited for EPR imaging and EPR microscopy. Multi-frequency EPR is a useful technique in itself [1], and a viable complement to other methods of spectroscopic investigations, such as NMR, conductivity, susceptibility measurements and infra-red spectroscopy. Exploitation of EPR spectra with multi-frequency EPR is helpful in discerning which mechanisms are operative in a particular sample [1]. Furthermore, this information can provide key insights for discriminating amongst competing models of relaxation processes, useful in elucidating structural and dynamical processes in a wide variety of systems. EPR spectra of polycrystalline and single crystals can show complicated frequency/magnetic field-dependent behavior.

In the early EPR literature, there are reported observations [2–4] of increase in EPR linewidth at lower frequencies, and its reduction at higher frequencies. Exchange narrowing occurs when the exchange interaction, $|J|$, expressed in frequency units, is much larger than the square-root of the second moment due to dipolar interactions at low resonance frequencies for a

paramagnetic system with identical spins. This happens because the fourth moment of the lineshape increases although the second moment remains the same for an isotropic exchange term, so that the EPR lineshape becomes narrowed at the center and extended in the wings.

There occurs broadening of EPR lines by the factor 10/3 due to the contribution of the non-secular terms of the dipole–dipole (d–d) interaction between the paramagnetic ions, when the average field of the dipolar interaction, H_{dd}, exceeds the resonant magnetic field, or in the case of exchange narrowing of dipole–dipole broadened line, if the exchange-interaction constant, $|J|$, exceeds the energy of the quantum of magnetic-resonance frequency. Increasing the resonance frequency causes narrowing of EPR lines, because then the 10/3 non-secular broadening does not occur as the non-secular terms of the d–d interaction become negligible. Accordingly, if other effects, e.g. internal fields, are negligible, occurrence of exchange-narrowed EPR spectrum as a function of magnetic-resonance frequency can be used to estimate $|J|$. To this end, measurements to verify these predictions were reported for frequencies $\leqslant 105$ GHz: (i) $Cu(NH_3)_4SO_4 \cdot H_2O$ single crystal at 300 K [5]: the observed linewidths being 11.5 G, 10 G, 9.5 G, 7.5 G, 7 G, 6 G, 5 G at 3, 9.5, 13, 21, 33, 50, 105 GHz, respectively, characterized by $|J| = 3.15$ K (~ 65 GHz); (ii) $K_2CuCl_4 \cdot 2H_2O$ single crystal [6]: the observed linewidths being 183, 175, 138, 115, 84, 80, 54, 40, 35 G at 3, 5, 9, 10, 16, 18, 23, 35, 46 GHz, respectively, characterized by $|J| = 0.24$ K (~ 5 GHz).

* Corresponding author. Fax: +1 514 848 2828.
E-mail address: skmisra@alcor.concordia.ca (S.K. Misra).

Recently, with the advent of very high-frequency (VHF, >140 GHz) EPR spectrometers, the prediction of exchange narrowing with increasing frequency for samples with $|J| > 100$ GHz can be seriously tested. As well, for concentrated samples containing identical paramagnetic ions, the exchange interaction can be estimated by multi-frequency measurements by finding the frequency above which exchange narrowing occurs provided that other broadening effects are negligible, e.g. internal fields due to other paramagnetic ions in the vicinity. With the recent availability of high-frequency spectrometers, this project started with the objective to explore the 10/3-exchange narrowing of an EPR line with increasing frequency [2], including VHF frequencies, e.g. at frequencies of 9.6 (X-band), 35.7 (Q-band), 95 (W-band), 190, 288, and 387 GHz. To this end, the system of $MnSO_4 \cdot H_2O$ was chosen. Contrary to the expectation, no narrowing of EPR line was found with increasing frequency, instead a distortion/splitting of EPR line was found. A similar effect has been reported in K_3CrO_8 crystal by Cage et al. [7,8].

The effect of internal fields on lineshape in HFHF EPR in samples concentrated in paramagnetic spins can be very profound due to resulting g-shifts, associated with modifications of lineshapes. One relevant example reported in the literature is that of the EPR spectrum of the paramagnetic ion Cr^{5+} (electron spin $S = \frac{1}{2}$, nuclear spin $I = 0$) in a single crystal of K_3CrO_8 in a variable-frequency measurement in the range 1–370 GHz, observing splitting of EPR lines at 370 GHz by Cage et al. [8] in K_3CrO_8. The interpretation of spectra was made in terms of the exchange narrowing of EPR signal in solids, based on a simple Hamiltonian. It was found that the linewidth decreased monotonically as a function of frequency from 1 to about 100 GHz, which then started to increase as the frequency was increased. These data were compared with those on a magnetically diluted spin system in diamagnetic K_3NbO_8, containing ~0.5 mol% of K_3CrO_8, taking into account the broadening effect of the magnetic-field dependent terms, e.g. broadening due to g-strain and magnetization of the sample holder and waveguide up to 14 T for a meaningful interpretation. The K_3CrO_8 linewidths were analyzed in terms of Anderson–Weiss model [4], taking into account the various line-broadening effects. They found agreement, within 5%, for the exchange constant J (=1.35 K) and about 25% for the dipolar field H_p (=16 mT) [8]. Nevertheless, they noted some deviations and unusual splitting in the EPR spectrum at 370 GHz in K_3CrO_8, whose origin they could not identify. In a subsequent measurement in undiluted Cr^{5+} salts at 375 GHz [8], they interpreted the broadening of the EPR peaks due to g-strain, and found better resolution enhancement with increasing applied Zeeman field up to 14 T, which was so significant that a single unresolved peak at fields less than 1 T became split into its three g-tensor components at fields greater than 10 T. No attempts were made in Refs. [7,8] to interpret data in terms of internal fields due to paramagnetic spins in the vicinity at sufficiently high magnetic field, bringing into existence different g-shifts for different Cr^{5+} ions in the sample, associated with their particular modified lineshapes.

According to the theory presented below in Section 2, this is due to an overlap of EPR lineshapes due to different g-shifts, being proportional to B/T, where B is the intensity of the external magnetic field and T is the temperature. This manifests in splitting, or distortion, of EPR lineshape at high magnetic fields, a phenomenon that does not occur at low magnetic fields used in low-frequency (LFLF) EPR.

It is the purpose of this paper (i) to provide a theoretial treatment for the calculation of EPR lineshape as affected by interactions with the paramagnetic ions in the vicinity; and (ii) to apply this theory to analyze multifrequency, including HFHF EPR data. This will include (a) data on $MnSO_4 \cdot H_2O$ powder samples with varying concentrations of Mn^{2+} ions; and (b) data on a K_3CrO_8

single crystal. In both these cases, involving samples concentrated in paramagnetic spins, the paramagnetic spins experience significant g-shifts at high magnetic fields due to the internal fields produced by the paramagnetic ions in their vicinity in the sample. The resulting EPR spectrum for the various ions is then an overlap of different EPR lineshapes situated at different values of the external magnetic field. This has been verified here by simulation of EPR spectra taking into account appropriate g-shifts due to internal fields and Lorentzian and/or Gaussian lineshapes for the various ions. In addition, the published spectrum of K_3CrO_8 single crystal at 370 GHz [8] has been satisfactorily simulated here as an overlap of EPR spectra, characterized by their different lineshapes, situated at different values of the external magnetic field due to different internal fields from clusters of paramagnetic spins situated in their environments in the crystal.

2. Theory

2.1. Calculation of internal field and lineshape due to a cluster of paramagnetic spins

The model for calculation that will be used here is as follows. When the intensity of the external magnetic field (B) is sufficiently high, a paramagnetic spin in the sample experiences an effective field at its site: $B_e = B + B_{int}$, where B_{int} is the internal magnetic field at its site induced by the paramagnetic spins in the vicinity. Furthermore, these interactions also modify its lineshape. Since EPR is sensitive to the environment of a paramagnetic spin, different paramagnetic ions in the sample experience their particular B_e and lineshapes, which can be approximated by a particular composition of Gaussian and Lorentzian shapes.

The calculation of the effect of paramagnetic ions in the vicinity on the line position and lineshape of a paramagnetic spin is described below, following the considerations of Kambe and Usui [9] in the nuclear context.

2.1.1. Spin hamiltonian

The system to be considered is a spin S_0 interacting with a cluster of m spins S_i ($i = 1, 2, 3, \ldots, m$), so that the spin Hamiltonian is the sum of its spin Hamiltonian, H_0, as well as pair-wise interactions with the spins of the cluster, H_{0i}, as follows:

$$H = H_0 + \sum_i H_{0i}; \quad i = 1, 2, \ldots, m, \tag{1}$$

with

$$H_0 = \mu_B S_0 \cdot \tilde{g} \cdot B + H_{ZFS}. \tag{2}$$

where, the first term on the right hand side of H_0 in Eq. (2) is the Zeeman interaction with μ_B being the Bohr magneton and $\tilde{g}$ being the g-matrix, and the second term, H_{ZFS}, represents the zero-field splitting terms. The terms H_{0i} represent the pair-wise interaction between the spins S_0 and S_i, including both the exchange and dipolar interactions, described in more detail in Eq. (23) below.

2.1.2. EPR lineshape: moments

Under the action of a microwave field (B_1), the interaction Hamiltonian:

$$H_{int} = \mu_B S_0 \cdot \tilde{g} \cdot B_1, \tag{3}$$

induces resonant transitions when the quantum of microwave energy, $h\nu$, where h is Planck's constant and ν is the frequency of the microwave radiation, matches energy-level separation between a pair of energy levels E_n and $E_{n'}$, provided that the transition probability, $P_{nn'} = P_{n'n}$, is non-zero, which is, using "Fermi's golden rule", given by

$$P_{nn'} = \frac{1}{\hbar^2}|\langle n|H_{int}|n'\rangle|^2 \rho(v),$$

where $\hbar = h/2\pi$, and $\rho(v)$ is the density of states, so that $\rho(v)dv = dN(v, v + dv)$ is the number of states in the frequency interval dv about $v = |(E_{n'} - E_n)/h|$. The absorption coefficient $A(v)$, per unit frequency interval, taking into account the Boltzmann distribution of population, is defined as

$$A(v)dv = \frac{hv}{Z}\sum_n \left(e^{-\frac{E_n}{k_BT}} - e^{-\frac{E_{n'}}{k_BT}}\right)\sum_{n',+dv}\frac{2\pi}{\hbar^2}|\langle n|H_{int}|n'\rangle|^2, \quad (4)$$

where k_B is Boltzmann's constant. The second summation is over only those of n' states which satisfy the condition $hv \leqslant E_{n'} - E_n \leqslant h(v + dv)$; and Z is the partition function defined as $Z = \sum_n \exp(-E_n/kT) = Tr(\exp(-H/kT))$. The absorption coefficient is related to the imaginary part of the complex susceptibility, $\chi''(v)$, as follows: $A(v) = 8\pi^2 v\chi''(v)$. Then Eq. (4) becomes:

$$\chi''(v)dv = \frac{\pi}{hZ}\sum_n \left(e^{-\frac{E_n}{k_BT}} - e^{-\frac{E_{n'}}{k_BT}}\right)\sum_{n',+dv}|\langle n|H_{int}|n'\rangle|^2, \quad (5)$$

Eq. (5) contains the functional form of $\chi''(v)$. One can now calculate the moments of the EPR lineshape from Eq. (5). These turn out to be in the form of traces of expectation values of certain operators as seen below.

2.1.2.1. Zeroth moment (area under the absorption curve). It is given by

$$\int_0^\infty \chi''(v)dv = \frac{\pi}{hZ}\sum_n\sum_{n',+}\left(e^{-\frac{E_n}{k_BT}} - e^{-\frac{E_{n'}}{k_BT}}\right)|\langle n|H_{int}|n'\rangle|^2, \quad (6)$$

where the summation $\sum_{n',+}$ extends over all those n' for which $E_{n'} > E_n$. Alternatively, one can introduce the operators H_{int}^+ and H_{int}^-, so that $H_{int} = H_{int}^+ + H_{int}^-$, as follows:

$$\langle n|H_{int}^+|n'\rangle = \langle n|H_{int}|n'\rangle \text{ for } E_{n'} < E_n, = 0, otherwise, \quad (7a)$$

and

$$\langle n|H_{int}^-|n'\rangle = \langle n|H_{int}|n'\rangle \text{ for } E_{n'} > E_n; = 0, otherwise. \quad (7b)$$

Eq. (6) for the zeroth moment can now be transformed, using (7a) and (7b), in the form of a *trace*:

$$\int_0^\infty \chi''(v)dv = \frac{\pi}{hZ}\sum_n\sum_{n'}\begin{pmatrix}e^{-\frac{E_n}{k_BT}}\langle n|H_{int}^-|n'\rangle\langle n'|H_{int}^+|n\rangle - \\ e^{-\frac{E_n}{k_BT}}\langle n'|H_{int}^+|n\rangle\langle n|H_{int}^-|n'\rangle\end{pmatrix}$$
$$= \frac{\pi}{hZ}Tr\{(e^{-H/k_BT})[H_{int}^-, H_{int}^+]\} = \left\langle\frac{\pi}{hZ}[H_{int}^-, H_{int}^+]\right\rangle_T, \quad (8)$$

where $[A,B] = AB - BA$ and the symbol $\langle\rangle_T$ stands for the average at temperature T. The advantage of expression (8) is that since *Trace* is invariant under a transformation of basis, it can be calculated in any convenient representation. For the transition $n \leftrightarrow n'$, **H_{int}** would have non-zero matrix elements only between the levels with the energy difference $E_{n'} - E_n = hv; (E_{n'} > E_n)$.

2.1.2.2. First moment. It is given by

$$h\int_0^\infty v\chi''(v)dv = \frac{\pi}{hZ}\sum_n\sum_{n',+}(E_{n'} - E_n)\left(e^{-\frac{E_n}{k_BT}} - e^{-\frac{E_{n'}}{k_BT}}\right)|\langle n|H_{int}|n'\rangle|^2$$
$$= \frac{\pi}{2hZ}\sum_n\sum_{n',+}(E_{n'} - E_n)\left(e^{-\frac{E_n}{k_BT}} - e^{-\frac{E_{n'}}{k_BT}}\right)|\langle n|H_{int}|n'\rangle|^2$$
$$= \frac{\pi}{2hZ}Tr\{(e^{-H/k_BT})[H_{int}, [H, H_{int}]]\}$$
$$= \left\langle\frac{\pi}{2h}[H_{int}, [H, H_{int}]]\right\rangle_T \quad (9)$$

It is noted that in writing the second term in Eq. (9) the summation over $n' + dv$ has been changed to n', thereby introducing a multiplication factor of ½, since in this conversion the additional summation $n', -dv$ is equal to that over $n', +dv$.

2.1.2.3. Second moment. It is expressed as

$$h^2\int_0^\infty v^2\chi''(v)dv = \frac{\pi}{hZ}\sum_n\sum_{n',+}(E_{n'}$$
$$- E_n)^2\left(e^{-\frac{E_n}{k_BT}} - e^{-\frac{E_{n'}}{k_BT}}\right)|\langle n|H_{int}|n'\rangle|^2$$
$$= \frac{\pi}{hZ}Tr\{(e^{-H/k_BT})[[H_{int}^-, H], [H, H_{int}^+]]\}$$
$$= \left\langle\frac{\pi}{h}[[H_{int}^-, H], [H, H_{int}^+]]\right\rangle_T \quad (10)$$

2.1.2.4. Higher-order moments. Following the same procedure as that used above for the calculation of first- and second-order moments, it can be shown that the even- and odd-order moments can be written as:

$$\int_0^\infty (hv)^{2\ell}\chi''(v)dv = \frac{\pi}{h}\langle[\{H_{int}^-, H\}^\ell, {}^\ell\{H, H_{int}^+\}]\rangle_T \quad (11)$$

and

$$\int_0^\infty (hv)^{2\ell-1}\chi''(v)dv = \frac{\pi}{2h}\langle[\{H_{int}, H\}^{\ell-1}, {}^\ell\{H, H_{int}\}]\rangle_T, \quad (12)$$

respectively. In Eqs. (11) and (12), the symbols $\{\}^\ell$ and $^l\{\}$ represent the iterated commutators, as follows:

$$\{A, H\}^\ell = [[\cdots[[A, H], H], \cdots], H] \quad (13)$$

and

$${}^\ell\{H, A\} = [H, [H, [\cdots[H, A]\cdots]]] = (-1)^\ell\{A, H\}^\ell \quad (14)$$

In Eqs. (13) and (14) H appears ℓ times in a repetitive manner as indicated by the dots.

2.1.2.5. Some useful expressions. Using the above, some meaningful expressions can be obtained.

2.1.2.6. Mean frequency. It is defined as:

$$\langle v\rangle_{ave} = \int_0^\infty\int_0^\infty v\chi''(v)dv\chi''(v')dv'/\int_0^\infty \chi''(v)dv, \quad (15)$$

which is different from the original frequency, v_0, when the interaction with other paramagnetic spins is absent. The deviation of effective frequency is denoted as:

$$\langle\Delta_0 v\rangle = \langle v\rangle_{ave} - v_0. \quad (16)$$

This is equivalent to a shift in the effective resonant field by the amount

$$\Delta B_{res} = h\langle\Delta v_0\rangle/g\mu_B, \quad (17)$$

as a consequence of the *internal field* produced by a cluster of paramagnetic ions.

2.1.2.7. Linewidth. It can be expressed as the mean-square deviation about the mean frequency $\langle v\rangle_{ave}$:

$$\langle\Delta v^2\rangle_{ave} = \langle v^2\rangle_{ave} - \langle v\rangle^2. \quad (18)$$

To further simplify (18), the density matrix is now approximated as:

$$\rho = \exp(-H/k_BT) \approx \exp(-H_0/k_BT), \quad (19)$$

where the pair-wise interaction terms have been neglected.

Substituting Eqs. 1, 18, and 19 into Eqs. (8)–(10), one obtains for the zeroeth, first, and second moments

$$\int_0^\infty \chi''(v)dv = \frac{\pi}{h(Tr\rho_0)}Tr(\rho_0[H_{int}^-, H_{int}^+]) \tag{20}$$

$$\int_0^\infty (hv)\chi''(v)dv = \frac{\pi}{2h}\left\{ \begin{array}{l} \frac{1}{(Tr\rho_0)}Tr(\rho_0[H_{int},[H_0,H_{int}]]) \\ +\sum_i \frac{1}{(Tr\rho_0\rho_i)}Tr(\rho_0\rho_i)[H_{int},[T_{0i},H_{int}+H_{int}^i]] \end{array} \right\} \tag{21}$$

$$\int_0^\infty (hv)^2\chi''(v)dv = \frac{\pi}{h}\left\{ \begin{array}{l} \frac{1}{(Tr\rho_0)}Tr(\rho_0[[H_0,H_{int,i}^+],[H_0,H_{int,i}^-]]) \\ \sum_i \left(\frac{1}{(Tr\rho_0\rho_i)}Tr\left(\rho_0\rho_i \left\{ \begin{array}{l} [[T_{0i},H_{int}^++H_{int,i}^+],[H_0,H_{int}^-]]+ \\ [[H_0,H_{int}^+],[T_{0i},H_{int}^-+H_{int,i}^-]]+ \\ \frac{1}{2}[[T_{0i},H_{int}^++H_{int,i}^+],[T_{0i},H_{int}^-+H_{int,i}^-]] \end{array} \right\} \right) \right) \\ \sum_i \sum_{j(\ne i)} \frac{1}{(Tr\rho_0\rho_i\rho_j)}Tr(\rho_0\rho_i\rho_j[[T_{0i},H_{int}^++H_{int,i}^+],[T_{0j},H_{int}^-+H_{int,j}^-]]) \end{array} \right\} \tag{22}$$

In Eqs. (20)–(22),

$$\rho_i = \exp(-H_i/k_BT) \approx \exp(-H_0/k_BT),$$

where H_0 is the Hamiltonian of a paramagnetic spin, assuming that all spins are identical, in the absence of interaction with neighboring paramagnetic spins.

2.1.2.8. Detailed calculations of area (zeroth moment), internal field (first moment), and the linewidth (second moment). For these calculations, it is necessary to take into account the exchange and dipolar interactions included in H_{0i}, as expressed by Eqs. (1) and (2). As for the pair-wise interaction, H_{0i}, it can be simplified using the formalism of Van Vleck [10] as follows:

$$H_{0i} = A_{0i}S_0 \cdot S_i + B_{0i}S_{0z} \cdot S_{iz},$$

$$\text{where } A_{0i} = J_{0i} + \frac{\mu_B^2 g^2}{2r_{0i}^{+3}}(3\cos^2\theta_{0i} - 1), \tag{23}$$

$$\text{and } B_{0i} = -\frac{3\mu_B^2 g^2}{2r_{0i}^{+3}}(3\cos^2\theta_{0i} - 1).$$

In Eq. (23), J_{0i} is the exchange-interaction constant between the spins S_0 and S_i, r_{0i} is the distance between S_0, the paramagnetic ion being considered and S_i the i-th spin of the cluster it is interacting with; and $\cos\theta_{0i}$ is the direction cosine of r_{0i} with respect to the z-axis.

Introducing (23) into Eqs. (20)–(22), one obtains the following expressions:

Zeroth moment : $$\int_0^\infty \chi''(v)dv = -\frac{\pi}{2h}N\mu_B^2 g^2\langle S_{0z}\rangle_T \tag{24}$$

First moment : $$\int_0^\infty (hv)\chi''(v)dv$$
$$= -\frac{\pi}{2h}N\mu_B^2 g^2\langle S_{0z}\rangle_T[g\mu_B B + \langle S_{0z}\rangle_T\sum_i B_{0i}], \tag{25}$$

Second moment : $$\int_0^\infty (hv)^2\chi''(v)dv = -\frac{\pi}{2h}N\mu_B^2 g^2\langle S_{0z}\rangle_T$$
$$\times \left[\begin{array}{l} \left(g\mu_B B + \langle S_{0z}\rangle_T\sum_i B_{0i} \right)^2 \\ +(\langle S_{0z}^2\rangle_T - \langle S_{0z}\rangle_T^2)\sum_i B_{0i}^2 \end{array} \right], \tag{26}$$

In Eqs. (24)–(26), N is the total number of spins in the cluster.

Taking into account the Zeeman term only, and neglecting the exchange interaction, which is the case in HFHF EPR due to the

large magnitude of the required magnetic field, the following values are obtained for the expectation values of the spin component S_{0z} and S_{0z}^2, as follows:

$$\langle S_{0z}\rangle_T = \sum_{M=-S}^{M=S} Me^{-g\mu_B BM/k_BT} / \sum_{M=-S}^{M=S} e^{-g\mu_B BM/k_BT} = -SB_S(y) \tag{27}$$

and

$$\langle S_{0z}^2\rangle_T = \sum_{M=-S}^{M=S} M^2 e^{-g\mu_B BM/k_BT} / \sum_{M=-S}^{M=S} e^{-g\mu_B BM/k_BT} = S^2\left(B_S^2(y) + \frac{d}{dy}B_S(y)\right); \tag{28}$$

with $y = g\mu_B BS/k_BT$ and $B_S(y)$ is the Brillouin function:

$$B_S(y) = \frac{2S+1}{2S}\coth\left(\frac{2S+1}{2S}y\right) - \frac{1}{2S}\coth\frac{y}{2S} \tag{29}$$

2.1.2.9. g-Shift due to internal field. Finally, the g-shift as implied by the expression for the first moment, Eq. (25) is:

$$\Delta g = \frac{\langle S_{0z}\rangle_T}{\mu_B B}\sum_i B_{0i}, \tag{30}$$

As revealed by Eq. (34), the g-shift depends on the sum $\sum_i B_{0i}$ Using now (23) for B_{0i}, it can be expressed as:

$$\Delta g = -\frac{3}{2}\frac{\langle M_z\rangle_T g}{N_1 B}\sum_i \frac{1}{r_{0i}^{+3}}(3\cos^2\theta_{0i} - 1), \tag{31}$$

The sum in Eq. (31) depends on the shape of the sample, and

$$\langle M_z\rangle_T = \mu_B N_1\langle S_z\rangle_T, \tag{32}$$

where N_1 is the number of spins per unit volume. The sum in Eq. (31) becomes the classical demagnetization factor, N_z, when the shape is ellipsoidal, and is oriented such that one of its ellipsoidal axis is along the z-axis, the direction of the external magnetic field, so that

$$N_z = \frac{1}{N_1}\sum_i \frac{1}{r_{0i}^{-3}}(3\cos^2\theta_{0i} - 1) + \left(\frac{4\pi}{3}\right), \tag{33}$$

Then,

$$\Delta g = \frac{3}{2}\frac{\langle M_z\rangle_T g}{B}\left(\frac{4\pi}{3} - N_z\right)N_z = \frac{3\chi_0 g}{2}\left(\frac{4\pi}{3} - N_z\right), \tag{34}$$

In writing (32), the expression for the susceptibility

$$\chi_0 = \frac{\langle M_z\rangle_T}{B} \tag{35}$$

has been used.

Eq. (34) reveals that Δg increases as $\frac{B}{T}$ increases, first linearly, thereafter attaining a constant value as $\frac{B}{T} \to \infty$, being proportional to $B_S(g\mu_B BS/k_BT)$. [11] as given by Eqs. (29) and (32).

As a consequence, in HFHF experiments involving high magnetic fields, the g-shift of an EPR line becomes significant even at room temperature similar to the situation in LFLF EPR involving smaller magnetic fields, when the temperature is decreased sufficiently, e.g. liquid-helium temperatures. Likewise, the higher moments of the lineshape are affected significantly as $\frac{B}{T} \to \infty$, so that the overall lineshape in HFHF EPR is also modified significantly at room temperature

3. Experimental details

In this section are described experimental multifrequency EPR spectra of $MnSO_4 \cdot H_2O$ samples with varying paramagnetic concentrations, and that of K_3CrO_8 crystal in varying magnetic fields, to

show the enhanced effect of internal magnetic fields and modification of EPR lineshapes due to paramagnetic ions in the vicinity as the intensity of the external magnetic field is increased in HFHF EPR.

3.1. MnSO$_4$·H$_2$O powder

3.1.1. Samples

For EPR measurements extra high-purity commercially available MnSO$_4$·H$_2$O powder was used, whose magnetic susceptibility is $14,200 \times 10^{-6}$ cm^3/mol [12]. in addition, EPR spectra were also recorded on sufficiently diluted MnSO$_4$·H$_2$O powder by mixing it with diamagnetic KBr powder and/or vacuum grease to show that there is no splitting/distortion of EPR lines, because the Mn^{2+} micro-crystals constituting the polycrystalline sample are sufficiently apart from each other not able to induce any significant internal magnetic fields.

3.1.2. Spectrometers

Low-frequency X-band ($\sim$9.5 GHz) and Q-band ($\sim$35.7 GHz) spectra were recorded at room temperature on Bruker and Varian commercial spectrometers, respectively. As for HFHF EPR spectra, they were recorded on a home-built spectrometer at the EPR facility of NHMFL (National High Magnetic Field Laboratory, Tallahassee, Florida). The instrument was a transmission-type device in which microwaves are propagated in cylindrical light pipes. The microwaves were generated by a phase-locked Virginia-Diodes source generating a frequency of 13 ± 1 GHz and producing harmonics of which the 4th, 8th, 16th, 24th and 32nd were available. A superconducting magnet (Oxford Instruments) capable of reaching a field of 17 T was employed. The field was calibrated using DPPH, with $g = 2.0037$. The differences between 'calibrated' and 'uncalibrated' fields are 50–90 G. No resonance cavity was used. Detection was provided by a liquid-helium-cooled InSb hot-electron bolometer (QMC Ltd., Cardiff, UK). Magnetic-field modulation at 40 kHz and ca. 2 mT amplitude was employed. A Stanford SR830 lock-in amplifier was used to convert the modulated signal to a DC voltage.

3.2. EPR spectra

3.2.1. LFLF EPR

The X (9.595 GHz)- and Q (35.7 GHz)-band spectra are shown in Fig. 1. No distortion of lineshape is seen at these frequencies, which require low magnetic fields.

3.2.2. HFHF EPR

Two sets of measurements were performed. These are made to see the effect of varying concentrations of paramagnetic spins, by diluting the MnSO$_4$·H$_2$O powder with vacuum grease and diamagnetic KBr powder.

3.2.2.1. (a) Decreasing concentration dependence (diluted powder). In Fig. 2 are shown spectra on a diluted powder of MnSO$_4$·H$_2$O, mixed in vacuum grease with equal volume, at increasing frequencies of 94.64 (A), 190.52 (B), 288.22 (C), and 387.48 (D) GHz, respectively. The highest-frequency spectrum D, unlike the spectra A, B, and C which are undistorted, shows distortion of lineshape due to significant internal fields produced by paramagnetic ions in the vicinity at very high magnetic fields. EPR spectra were also recorded at the highest frequency for decreasing concentration of paramagnetic (Mn^{2+}) ions. Accordingly, the bottom two EPR spectra at 387.48 GHz (E and F) are for decreasing concentrations of MnSO$_4$·H$_2$O: (i) in grease by a factor of 2 (E), and (ii) by mixing the sample in (i) in diamagnetic KBr powder 20 times its volume
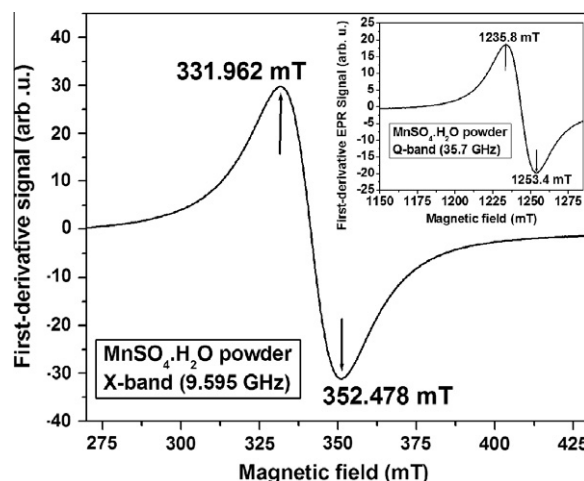

Fig. 1. EPR at low magnetic-fields: X-band (9.565 GHz) spectrum of a sample of MnSO$_4$·H$_2$O powder in the range 250–450 mT. The inset shows the spectrum at the low magnetic-field Q-band (35.7 GHz).

(F), respectively, as compared to that in D. It is seen that the shape distortion becomes smaller in E as compared to that in D, whereas it disappears entirely in F, exhibiting the same undistorted shape as those of A, B, and C, due to considerably reduced concentration of Mn^{2+} spins, so that the internal fields due to them are negligible.

3.2.2.2. Increasing concentration dependence (concentrated sample). Fig. 3 shows EPR spectra on MnSO$_4$·H$_2$O powder sample, mixed in one-half of its volume in vacuum grease, recorded at increasing microwave frequencies (magnetic fields) of 96.77 (A), 193.54 (B), 290.33 (C), and 387.084 GHz (D–F). They are shown in Fig. 3. The spectra E and F at 387.084 GHz are from those samples of MnSO$_4$·H$_2$O, in which mixing with grease was in such amounts that the concentration of MnSO$_4$·H$_2$O was increased by factors of 8 (E) and 40 (F), specifically to see the effect of increased concentrations of paramagnetic ions. When comparing the spectra A, B, C, D with each other, it was found that there was no distortion of lineshape for frequencies below 387.084 GHz, whereas at 387.084 GHz there was, indeed, seen a distortion of the EPR lineshape due to the paramagnetic (Mn^{2+}) ions in the vicinity. When the concentration of MnSO$_4$ was increased by factors of 8 (E) and 40 (F), further distortions of lineshapes were seen at 387.084 GHz, increasing with the concentration.

These concentration-dependent EPR spectra show that the resulting EPR lineshape in MnSO$_4$·H$_2$O powder is quite sensitive to the interactions with the paramagnetic ions in their vicinities, that is to the internal magnetic fields produced by the paramagnetic ions in the vicinity, associated with modified lineshapes. With sufficient dilution the distortion of the lineshape disappears, as the interactions with the paramagnetic ions in the vicinity become negligible due to not being sufficiently close to affect the position and EPR lineshape.

3.3. K$_3$CrO$_8$ single crystal

The preparation of K$_3$CrO$_8$ single crystals and susceptibility measurements are described by Dalal et al. [13]; see also Refs. [7,8]. The susceptibility was measured to be ca. 1250×10^{-6} cm^3/mol The Cr^{5+} spectrum at 387 GHz on a single crystal of K$_3$CrO$_8$, as reported by Cage et al. [8], is shown in Fig. 5, which also includes simulated spectra as described below in Section 4. The details of the spectrometer used are described in Refs. [7,8].
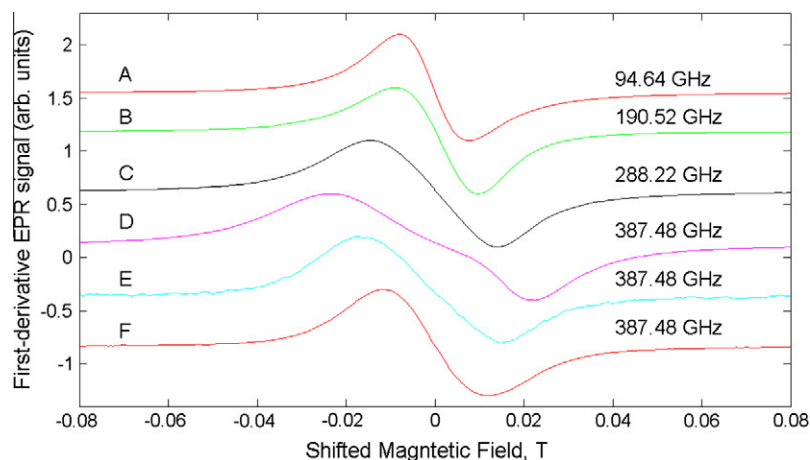
Fig. 2. EPR at very high magnetic-fields: EPR spectra of a sample of $MnSO_4 \cdot H_2O$ powder sample mixed with grease at increasing frequencies of 94.64 (A), 190.52 (B), 288.22 (C), and 387.48 (D–F) GHz. Two more spectra are recorded at the highest frequency 387.48 GHz (E and F) with decreased concentration of $MnSO_4 \cdot H_2O$: (E) by a factor of 2 in grease, and (F) by an additional factor of 20 in diamagnetic KBr powder, respectively, as compared to that in D. The magnetic fields have been shifted so that the centers of the lines at different frequencies match. (The center field can be calculated using the formula $B_0 = h\nu/(2.0023\mu_B)$).
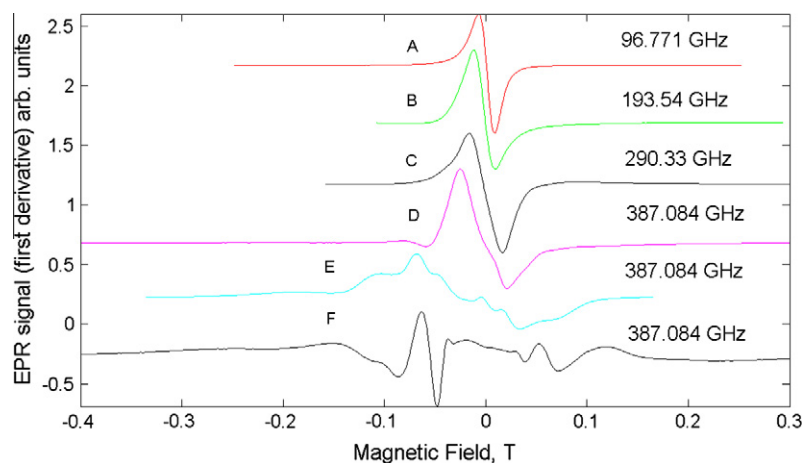

Fig. 3. EPR at very high magnetic-fields: EPR spectra of a sample of $MnSO_4 \cdot H_2O$ powder sample mixed with grease at increasing frequencies of 96.78 (A), 193.54 (B), 290.33 (C), and 387.08 (D–F) GHz. Two more spectra are recorded at the highest frequency 387.08 GHz (E and F) with increased concentration of $MnSO_4 \cdot H_2O$ in grease: (E) by a factor of 8, and (F) by a factor of 40, respectively, as compared to that in D. The magnetic fields have been shifted so that the centers of the lines at different frequencies match. (The center field can be calculated using the formula $B_0 = h\nu/(2.0023\mu_B)$).

4. Simulations of EPR spectra for $MnSO_4 \cdot H_2O$ powder and K_3CrO_8 single crystal

This section describes simulations to show that the $MnSO_4 \cdot H_2O$ powder and K_3CrO_8 single-crystal spectra observed at 387 and 370 GHz, respectively, can be reproduced to be superposition of EPR spectra due to interactions with paramagnetic ions in the vicinity producing different internal magnetic fields, as reflected in the effective g-values of the superposing EPR lines, associated with their particular lineshapes. The simulations were performed using the software SPIN [14], which uses diagonalization of the spin-Hamiltonian matrix to calculate the EPR lineshape, using the g-values and the nature of line, e.g. Gaussian, lorentzian, or a mixture of the two. The details of simulations of the lineshapes and effective g-values for the two samples are as follows.

4.1. $MnSO_4 \cdot H_2O$ powder

The Mn^{2+} ion possesses the electron spin $S = 5/2$ and nuclear spin $I = 5/2$. In a powder sample concentrated in spins, as in the present case, only the central fine-structure transition $\frac{1}{2} \leftrightarrow -\frac{1}{2}$ is

observed, the outer fine-structure transitions are completely broadened out [2]. Furthermore, the hyperfine splitting is not all resolved. It can therefore be treated as a spin-1/2 system for the purposes of simulation, assuming an effective isotropic g-value. The observed spectrum, distorted in shape, D, of Fig. 2 (shown by a continuous line in Fig. 4), recorded at 387.48 GHz, was satisfactorily simulated by trial-and-error, as an overlap of only two EPR lines (lines 1 and 2 in Fig. 4) with about the same intensity, characterized by different effective g-values that take into account the internal fields due to two sets of paramagnetic ions in the vicinity, with Gaussian lineshapes associated with Lorentzian components, whose details, e.g. the effective g-value, linewidth, nature of lineshape – Lorentzian or Gaussian or a mixture of the two, are listed in Table 1,

4.2. K_3CrO_8 single crystal

The Cr^{5+} ion possesses the electron spin $S = \frac{1}{2}$, along with the ^{53}Cr nucleus possessing the spin $I = 3/2$, with natural abundance of 9.55%; however, the hyperfine structure was not resolved due to high concentration of Cr^{5+} ions in the crystal. An effective
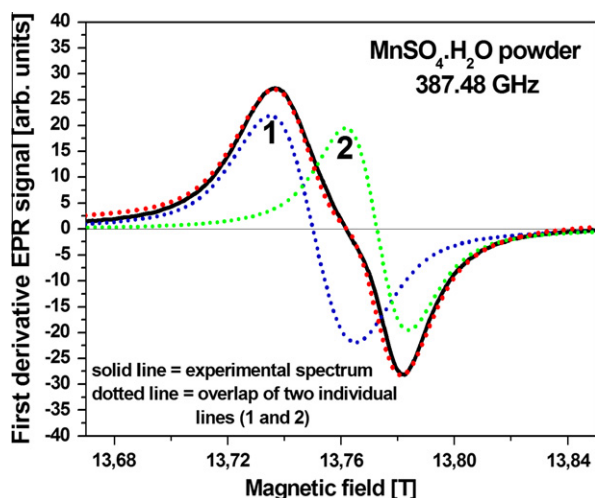
Fig. 4. The experimental (solid line) and simulated (dotted, superimposed on the experimental spectrum) lineshape to reproduce the experimentally observed EPR spectrum at 387.48 GHz in MnSO$_4$·H$_2$O powder over the magnetic-field range ~13.67–13.85 T. The parameters (g-values, line width, % of Gaussian in Lorentzian lineshape) of the two individual lineshapes (dotted 1 and 2), whose overlap produces the experimental spectrum satisfactorily, are listed in Table 1.

Fig. 5. The experimental and simulated lineshape to reproduce the experimentally observed EPR spectrum in K$_3$CrO$_8$ single crystal at 370.7 GHz over the magnetic-field range ~13.32–13.34 T. The parameters (g-values, line with, % of Gaussian in Lorentzian lineshape) of the individual lineshapes (dotted lines 1–8), whose overlap (dashed line) produces the experimental spectrum satisfactorily, are listed in Table 2.

Table 1
The parameters of the two EPR lineshapes (1 and 2 in Fig. 4), overlapped to constitute the observed spectrum D of Fig. 2 (solid line in Fig. 4) of MnSO$_4$·H$_2$O. The colors represent the individual lines as shown in Fig. 4. The plotted g-value takes into account the shift due to the internal field due to clusters of paramagnetic ions in the vicinity.

Number of individual EPR lineshape (from right to left)	g-Value	Linewidth (Gauss)	% Gaussian (in Lorentzian lineshape)
1	2.0108	150	50
2	2.0075	110	30

Table 2
List of the parameters of the individual lineshapes, whose overlap constitutes the simulated lineshape (red, dashed in Fig. 5). The relative height in the last column is with respect to the peak-to-peak total height of the experimental lineshape. The plotted g-value takes into account the shift due to the internal field due to clusters of paramagnetic ions in the vicinity.

Number of individual EPR lineshape (from right to left peak-wise)	g-Value	Linewidth (Gauss)	% Gaussian (in Lorentzian lineshape)	Relative height (%)
1	1.987200	20	75	12.29
2	1.987000	20	75	10.28
3	1.986920	4.1	75	27.84
4	1.986820	4.3	75	42.19
5	1.986800	5.5	75	19.42
6	1.986710	5.0	75	94.79
7	1.986527	11.5	100	81.16
8	1.986440	5	75	9.64

isotropic g-value was assumed for interaction with each paramagnetic cluster in the vicinity. The observed spectrum, black continuous line, with baseline correction, recorded on the K$_3$CrO$_8$ single crystal at 370.7 GHz, is shown in Fig. 5. It was satisfactorily simulated as shown by red, dotted line in Fig. 5, overlapping the observed spectrum, by trial-and-error, as an overlap of eight EPR lineshapes, denoted as 1–8 in Fig. 5, with Gaussian lineshapes associated with Lorentzian components, with varying intensities, whose details, e.g. the effective g-value, linewidth, nature of lineshape – Lorentzian or Gaussian or a mixture of the two, are listed in Table 2. The simulated lineshape (red, dotted line superposing the experimental spectrum) fits the experimental lineshape quite well in the relevant field range.

5. Discussion and concluding remarks

In general, one requires all moments of the lineshape to describe it completely. However, their calculation is unwieldy, and not really necessary. In practice, it is sufficient to calculate only the first (position of line) and second (linewidth) moments. It is clear from the simulations presented in this paper that as a result of interaction with paramagnetic ions in the vicinity the resonant field will be shifted at high magnetic fields from that in the absence of it. As well, the lineshape, that includes the linewidth, will be correspondingly affected. Different ions in the sample will see different shifts and lineshapes corresponding to interactions with the paramagnetic ions in their environments, which overlap each other to produce the observed EPR lineshape.
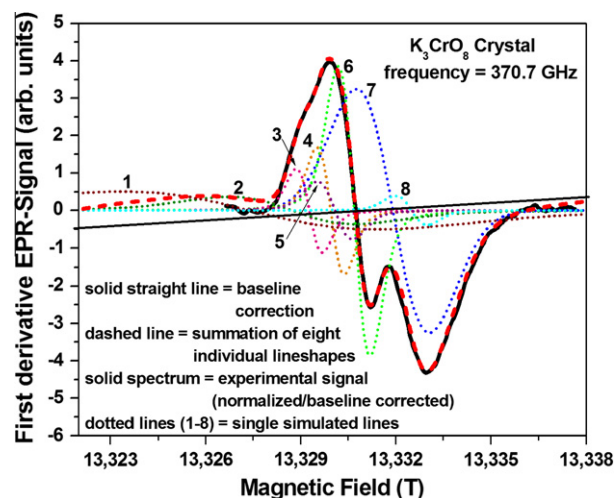
In the expressions for the various moments there appears the quantity B/T, e.g. in Eqs. (27)–(29), as discussed at the end of Section 2, so that the effect of interaction with a paramagnetic cluster becomes large as the magnetic field increases keeping the temperature constant, or as the temperature decreases keeping the field constant, or both with increasing field and decreasing temperature. For example, in going from X-band (~9.5 GHz) to the infra-red band at ~250 GHz, there is an increase in the external field by a factor of ~25 at room temperature. This is equivalent to the same effect as that would be obtained by the temperature decreasing from room temperature (295 K) to ~6 K at X-band. As a consequence, the "g-shift", which becomes significant at the relatively low magnetic field of X-band only at low temperatures, can now be observed at room temperature by increasing appropriately the frequency of the microwave field, or equivalently the magnitude of the magnetic field.

The data presented in this paper, and their analysis, confirmed by selected examples from many simulations of similar HFHF spectra not shown here, confirm that at sufficiently high magnetic fields, there appear significant internal magnetic fields at the sites of paramagnetic ions over and above the external magnetic field due to clusters of paramagnetic ions in their vicinity. They are

significant even at room temperature in HFHF EPR, involving very high external magnetic fields. When this happens the EPR line-shape becomes distorted, or even split up depending upon the conglomerate of paramagnetic clusters in the vicinity of the various paramagnetic ions. This effect should be taken into account when analyzing high-field EPR lineshapes. For example, Shin et al. [15] reported the observation of unexplained EPR lines at the high field of ca. 8.9 T at 250 GHz, not seen at the low magnetic field of ca. 0.35 T at 9.5 GHz, apparently due to the presence of internal fields at the paramagnetic ions due to clusters of paramagnetic ions in the sample at 250 GHz in Cs^+ (18-crowis-6)$_2X^-$, where $X^- = e^-$, Na^-, or Cs^- ($S = \frac{1}{2}$, $I = 1$). Similar high-field effects have been reported by Budil et al. [16].

Acknowledgments

References

[1] S.K. Misra (Ed.), Multifrequency Electron Paramagnetic Resonance: Theory and Applications, Wiley-VCH, Weinheim, Germany, 2011. Chapter 2.
[2] A. Abragam, B. Bleaney, Electron Paramagnetic Resonance of Transition Metal Ions, Oxford University Press, 1970.
[3] C.J. Gorter, J.H. Van Vleck, Phys. Rev. 72 (1947) 1128.
[4] P.W. Anderson, P.R. Weiss, Rev. Mod. Phys. 25 (1953) 269.
[5] R.N. Rogers, F. Carboni, P.M. Richards, Phys. Rev. Lett. 18 (1967) 1016.
[6] A.J. Henderson Jr., R.N. Rogers, Phys. Rev. 152 (1966) 218.
[7] B. Cage, A.K. Hassan, L. Pardi, J. Krzystek, L-C Brunel, N.S. Dalal, J. Magn. Reson. 124 (1997) 495.
[8] B. Cage, P. Cevec, R. Blinc, L-C Brunel, N.S. Dalal, J. Magn. Reson. 135 (1998) 178.
[9] K. Kambe, T. Usui, Prog. Theo. Phys. (Japan) 8 (1952) 302.
[10] J.H. van Vleck, Phys. Rev. 74 (1948) 1168.
[11] G.E. Pake, T.E. Estle, The Physical Principles of Electron Paramagnetic Resonance, W.A. Benjamin, Inc., Reading, Massachusetts, 1973. pp. 8,9.
[12] Landolt-Bernstein, Numerical data and functional relationships in science and technology, New Series, II/2, II/8, II/10, II/11, and II/12a, Coordination and Organometallic Transition Metal Compounds, Springer-Verlag, Heidelberg, 1966–1984.
[13] N.S. Dalal, J.M. Millar, M.S. Jagadeesh, M.S. Seehra, J. Chem. Phys. 74 (1980) 1916.
[14] A. Ozarowski, SPIN Software. Private Communication, 2006.
[15] D.H. Shin, J.L. Dye, D.E. Budil, K.A. Earle, J.H. Freed, J. Phys. Chem. 97 (1993) 1213.
[16] D.E. Budil, K.A. Earle, W.B. Lynch, J.H. Freed, in: A.J. Hoff (Ed.), Advanced EPR Applications in Biology and Biochemistry, Elsevier, Amsterdam, 1989 (Chapter 8).